

QCD Phase Diagram at finite Magnetic Field and Chemical Potential: A Holographic Approach Using Machine Learning

Rong-Gen Cai^{b,c,d}, Song He^{a,c,e}, Li Li^{c,d,f} and Hong-An Zeng^a

^a*Center for Theoretical Physics and College of Physics, Jilin University, Changchun 130012, People's Republic of China*

^b*School of Physical Science and Technology, Ningbo University, Ningbo, 315211, China*

^c*CAS Key Laboratory of Theoretical Physics, Institute of Theoretical Physics, Chinese Academy of Sciences, Beijing 100190, China*

^d*School of Fundamental Physics and Mathematical Sciences, Hangzhou Institute for Advanced Study, UCAS, Hangzhou 310024, China*

^e*Max Planck Institute for Gravitational Physics (Albert Einstein Institute), Am Mühlenberg 1, 14476 Golm, Germany and*

^f*School of Physical Sciences, University of Chinese Academy of Sciences, Beijing 100049, China.**
(Dated: June 19, 2024)

By leveraging neural networks, we address the inverse problem of constructing a quantitative 2+1-flavor holographic QCD model based on state-of-the-art lattice QCD data. Our model demonstrates quantitative agreement with the latest lattice QCD results. We construct the full phase diagram at finite magnetic field B , baryon chemical potential μ_B and temperature T . We uncover rich phase structure with a first-order phase transition surface and a critical endpoint line within the 3-dimensional phase diagram. The critical endpoint at vanishing chemical potential aligns with current speculations in the lattice QCD literature. In particular, for large magnetic field, we find two critical endpoints in the T - μ_B plane. The critical exponents of the critical endpoints adhere to scaling relations and depend on the background magnetic field. Moreover, they exhibit deviations from mean-field theory, highlighting the distinctive features of our holographic approach.

Introduction—Quantum Chromodynamics (QCD), the theory governing strong interactions, presents substantial theoretical and experimental challenges [1–3], particularly in the strongly coupled regime. The QCD phase diagram delineates various states of QCD matter under extreme conditions. It is critical for understanding phenomena ranging from heavy-ion collisions and astrophysics to cosmology. After decades of hard work and unremitting efforts, it has arrived at a sketchy phase diagram on QCD matter at finite temperature T and baryon chemical potential μ_B . At low chemical potentials, QCD undergoes a thermal crossover from a deconfined, chirally symmetric high-temperature phase to a hadronic phase of color-neutral bound states at low temperatures. This transition has been well-understood theoretically in particular from lattice QCD and confirmed experimentally. At large μ_B , effective field theories suggest that the crossover would end in a critical endpoint (CEP) beyond which these two phases are separated by a first-order transition.

The magnetic field B occurs naturally in non-central heavy-ion collisions, magnetars, and the early universe, thus becoming an indispensable part of understanding the properties of QCD matter [4]. The magnetic shift in the QCD phase diagram is crucial for studying strong interactions, particularly in intense magnetic environments and should impact the critical temperature for phase transitions, providing valuable insights into high-energy physics experiments and theoretical studies. At zero μ_B , a speculative phase diagram in a background magnetic field predicts the appearance of a critical line with CEP

above a critical magnetic field, similar to the T - μ_B phase structure at $B = 0$. Thus far, little is known about the phase diagram at both finite μ_B and B which is common in heavy-ion collisions and magnetars. The first principle lattice QCD fails at finite μ_B due to the notorious sign problem, and no significant evidence for the CEP has been obtained in the experimentally accessible region.

Locating the CEP and understanding its properties plays a key role in unveiling the mysteries of the QCD phase diagram. This has spurred research into the hot QCD at finite μ_B and B using effective field theories. Nevertheless, effective field theory methods like the Nambu-Jona-Lasinio models, quark models, Dyson-Schwinger equations, and Functional Renormalization Group have limitations when applied to study magnetic field effects. These methods often lack gauge invariance, require significant computational resources, and face challenges in capturing the complex dynamics introduced by magnetic fields [5]. To avoid such difficulties, a novel approach to model the properties of QCD is gauge/gravity duality which provides a powerful non-perturbative approach for solving strongly coupled non-Abelian gauge theories in terms of classical gravity degrees of freedom and their dynamics. Remarkable progress has been made in applying this holographic approach to the hot and dense QCD [6–8]. In the spirit of effective field theory, all free parameters in the gravity models are fixed by fitting to available data from both lattice simulations and experiments. In holographic studies, the construction of the QCD phase diagram in the T - μ_B plane began with [9–11], using the Einstein-Maxwell-

Dilaton (EMD) theory. Since then, various attempts have been made to refine the phase diagram [6, 12–19]. Few studies [8, 12, 20] tried to incorporate magnetic fields to align with lattice QCD-based equations of state. To develop a quantitative and effective holographic model that captures magnetic aspects of realistic QCD, one must apply available lattice QCD data to constrain magnetic coupling—an unsolved inverse problem.

In this work, we construct the first quantitative 2+1-flavor holographic QCD model to describe the magnetic effects on the hot and dense QCD, where all parameters are fixed using state-of-the-art lattice QCD data both at vanishing chemical potential $\mu_B = 0$ [21] and vanishing magnetic field $B = 0$ [22]. Fixing the gravity models is an enormous challenge for which we introduce a systematic algorithm involving neural networks. All thermodynamic quantities are computed directly from the holographic renormalization and the so-called thermodynamic consistency relations [23]. Our prediction for the thermodynamic observables at finite B is in quantitative agreement with the latest lattice results. Remarkably, we then manage to make precise predictions for the QCD phase diagram at strong coupling at finite B , T , and μ_B . We confirm the speculative phase structures in the T - μ_B plane at $B = 0$ and T - B plane at $\mu_B = 0$, for which a first-order transition line ends in a CEP. Surprisingly, for sufficiently large B , we find that the phase diagram in the T - μ_B plane develops two CEPs, far above expectations. In addition to the phase diagram, we study the critical behavior near the CEPs. The critical exponents satisfy the scaling relation but their values depend on the location of the CEPs.

Holographic model—To incorporate the essential QCD dynamics at finite magnetic field, temperature, and baryon chemical potential using the holographic description, the five-dimensional Einstein-Maxwell-Dilaton theory with a minimal field set reads

$$S = \frac{1}{2\kappa_N^2} \int d^5x \sqrt{-g} \left[\mathcal{R} - \frac{1}{2} \nabla_\mu \phi \nabla^\mu \phi - \frac{Z(\phi)}{4} F_{\mu\nu} F^{\mu\nu} - \frac{\hat{Z}(\phi)}{4} \hat{F}_{\mu\nu} \hat{F}^{\mu\nu} - V(\phi) \right], \quad (1)$$

where κ_N^2 is the effective Newton constant. The metric $g_{\mu\nu}$ characterizes the spacetime geometry, and the real scalar field ϕ encodes the breaking of conformal symmetry. The Maxwell field A_μ provides the finite baryon number density, while the magnetic field B is given by another Maxwell field \hat{A}_μ . The three functions $Z(\phi)$, $\hat{Z}(\phi)$, and $V(\phi)$ are crucial for describing real QCD and will be systematically fixed by matching to the lattice QCD data.

The bulk hairy black hole solutions are given as:

$$ds^2 = -f(r)e^{-\eta(r)} dt^2 + \frac{dr^2}{f(r)} + r^2(dx^2 + dy^2 + g(r)dz^2),$$

$$\phi = \phi(r), \quad A = A(r)dt, \quad \hat{A} = \frac{B}{2}(xdy - ydx), \quad (2)$$

where r is the holographic radial coordinate, the asymptotic anti-de Sitter boundary is at $r \rightarrow \infty$, and the event horizon is located at finite $r = r_h$. Note that the constant magnetic field in the z -direction breaks the isotropy. After solving the bulk equations of motion, we can read off all relevant quantities by the standard holographic dictionary, including the free energy density Ω , energy density ϵ , entropy density s , baryon number density n_B and magnetization M , see Appendix A for more details. In this sense, the gravity dual provides a first-principle description of QCD dynamics.

Machine learning—Since there is no first principle for fixing the couplings in our bottom-up model, constructing a quantitative effective holographic model requires the application of available lattice QCD data to constrain the coupling functions, a problem known as the inverse problem. As the increasing of lattice QCD data for both finite B and μ_B , it is almost impossible to manually re-tune the control parameters. To address this challenge, we propose a systematic algorithm involving a neural network taking advantage of its inverse propagation process.

For definiteness and without loss of generality, we illustrate the main idea for determining the magnetic coupling $\hat{Z}(\phi)$ using the neural network approach with other parameters fixed by matching to the lattice data at $\mu_B = B = 0$ [21]. The neural network is integrated into the Einstein equations derived from the action (1). Applying standard holographic duality, appropriate boundary conditions are set at both the ultraviolet (UV) boundary and event horizon. Numerical solutions are obtained with the given initial $\hat{Z}(\phi)$, leading to a trial equation of state derived through the standard holographic renormalization. This trial equation of state is then compared with lattice QCD data to measure the deviation between the two. This deviation is quantified through a loss function and we apply an optimization algorithm to minimize the loss function to find the optimal magnetic coupling. The detailed steps of this algorithm and its core techniques are outlined in Appendix B, providing a systematic approach to solving the inverse problem. Using this method, we constructed a holographic QCD model that aligns closely with lattice QCD results [22] at finite B but vanishing chemical potential. We shall set $e = 1$ in our present work.

Similar approach is used to obtain $Z(\phi)$ and $V(\phi)$ by matching the lattice data [21, 28] at $B = 0$. Surprisingly, the resulting profiles can be fitted very well by the one

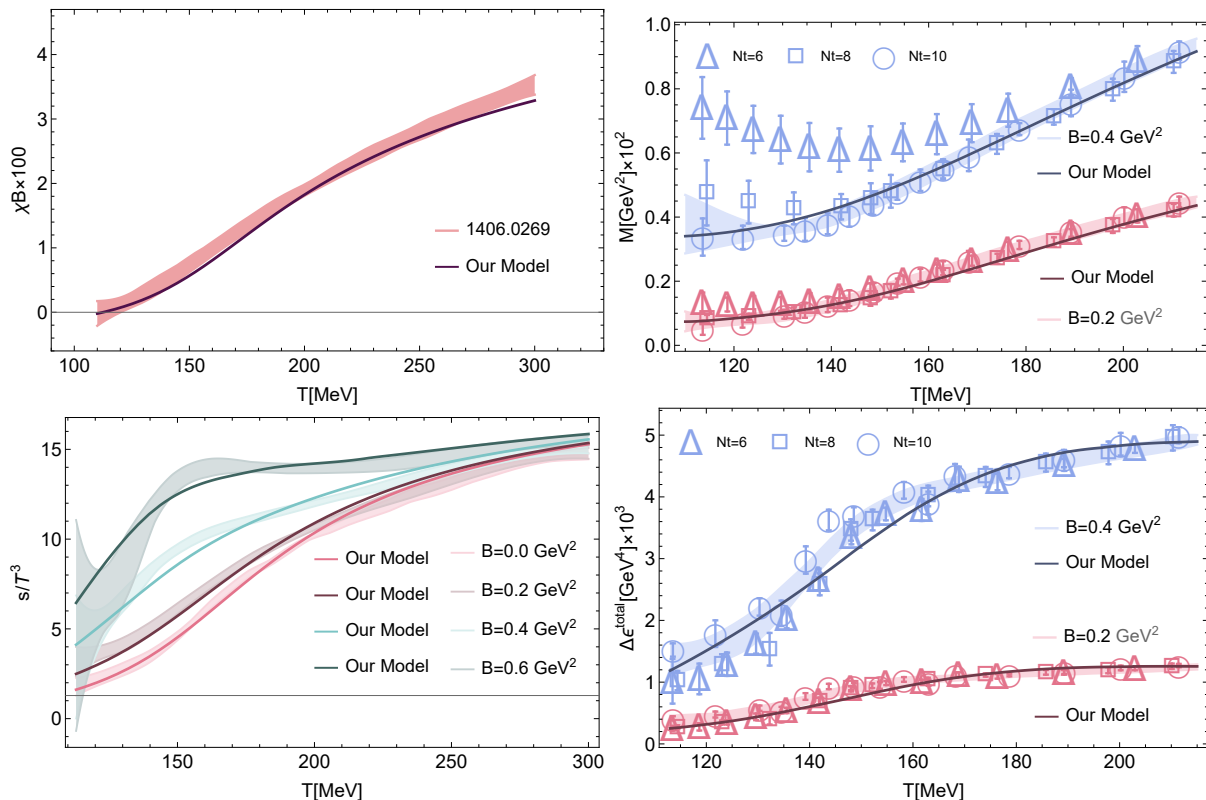


FIG. 1. Comparison of thermodynamic quantities obtained from our holographic QCD model with lattice QCD data [22]. It involves the magnetic susceptibility (upper left), magnetization (upper right), entropy density (lower left), and energy density (lower right) as functions of temperature for different magnetic field strengths ($B = 0.0, 0.2, 0.4, 0.6 \text{ GeV}^2$). Symbols with error bars indicate the lattice data, and the shaded regions represent the continuum estimates. Solid lines depict our model's results. We work in units with $e = 1$.

we found in recent work [29].

$$\begin{aligned}
 V(\phi) &= -12 \cosh[c_1 \phi] + (6c_1^2 - \frac{3}{2})\phi^2 + c_2 \phi^6, \\
 Z(\phi) &= \frac{1}{1 + c_3} \text{sech}[c_4 \phi^3] + \frac{c_3}{1 + c_3} e^{-c_5 \phi},
 \end{aligned}
 \quad (3)$$

with $c_1 = 0.7100, c_2 = 0.0037, c_3 = 1.935, c_4 = 0.085, c_5 = 30$. It has passed through strict benchmark tests by directly comparing results on the equation of state with those from lattice QCD simulations [29] and exhibited consistency with experimental data from heavy ion collisions regarding baryon number fluctuations along chemical freeze-out [30]. For simplicity, we shall use the explicit form of $V(\phi)$ and $Z(\phi)$ of (3) in the present work.

Fig. 1 illustrates our holographic predictions for four independent quantities—magnetic susceptibility χ^B , magnetization M , entropy density s , and energy density $\Delta\epsilon$ —in comparison with lattice QCD data [22]. One finds a quantitative agreement with the lattice results for available magnetic fields, which strongly supports our holographic QCD model. As far as we know, this is the first holographic model that can quantitatively fit lattice data in a magnetic field up to $B = 0.6 \text{ GeV}^2$. In appendix B, we further check the corresponding trace anomaly and

the renormalized longitudinal pressure predicted by the holographic model align with the lattice QCD [22].

QCD phase diagram—With the model fully established, we are ready to construct the QCD phase diagram at finite B , T , and μ_B . More precisely, we compute the free energy density Ω as a function of B , T , and μ_B . One can check straightforwardly that the gravitational solutions satisfy the first law of thermodynamics $d\Omega = -sdT - n_B d\mu_B - MdB$. A first-order phase transition can be identified uniquely by the swallowtail behavior for Ω versus T . The phase diagram at $B = 0$ was presented in Fig. 3 of [29] and the first-order phase transition line terminates at $(T_C = 105 \text{ MeV}, \mu_C = 555 \text{ MeV})$. The phase structure in the T - B plane at vanishing chemical potential is presented in Fig. 2. There is a line of first-order phase transitions terminating at the CEP located at $(T_C = 89.6 \text{ MeV}, B = 1.6 \text{ GeV}^2)$, which aligns with current speculations in the lattice QCD literature [31].

The full phase diagram is depicted in Fig. 3. The pink area denotes the first-order phase transition surface, dividing the quadrant into two parts: the high-temperature region corresponds to the quark-gluon plasma, while the low-temperature region corresponds to the hadron gas

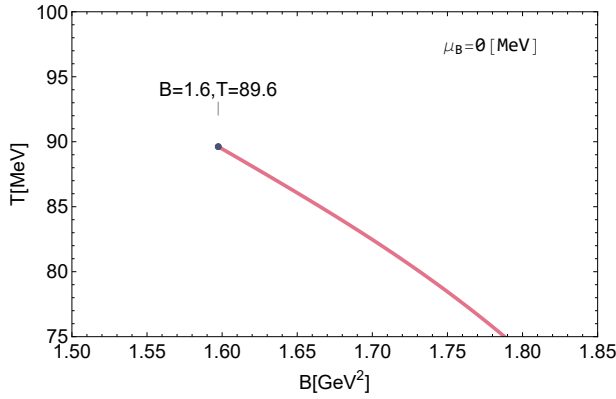


FIG. 2. The phase diagram on the $B - T$ plane at vanishing μ_B . The red dot denotes the CEP and the red line corresponds to the first order line.

phase. The red line in the diagram marks the location of CEP for various magnetic fields, where the first-order phase transition terminates and transitions into a smooth crossover at small chemical potentials.

Fig. 3 highlights three key observations:

1. As the magnetic field B increases up to $B = 1.618 \text{ GeV}^2$, the critical chemical potential μ_C at the CEP decreases, indicating that stronger magnetic fields shift the CEP to lower chemical potentials.
2. The critical temperature T_C at the CEP initially decreases with increasing B , reaching a minimum before increasing again. This turning point occurs around $T = 80 \text{ MeV}$, $B = 1.6 \sim 1.7 \text{ GeV}^2$, and $\mu_B = 0.2 \sim 0.28 \text{ GeV}$. This behavior suggests complicated effects in the presence of background magnetic field. It could be related to the inverse magnetic catalysis and magnetic catalysis reported in the literature.
3. At sufficiently strong magnetic field, multiple CEPs develop in the $T - \mu_B$ plane, as shown e.g. in Fig. 4. A first-order phase transition is observed for $0 < \mu_B < \mu_{C1}$ and $\mu_B > \mu_{C2}$, while a crossover occurs for $\mu_{C1} < \mu_B < \mu_{C2}$. As B increases, μ_{C1} and μ_{C2} converge to a single point. This reveals a rich phase structure in strong magnetic field and warrants further experimental verification.

Critical exponents—In addition to the phase diagram we study the critical behavior near the CEPs. Critical exponents characterize critical points in physical systems, for which thermodynamic properties typically exhibit power-law scaling with respect to temperature, chemical potential, or magnetic field. They are at the heart of the study of critical phenomena and provide insights into the critical behavior of QCD matter.

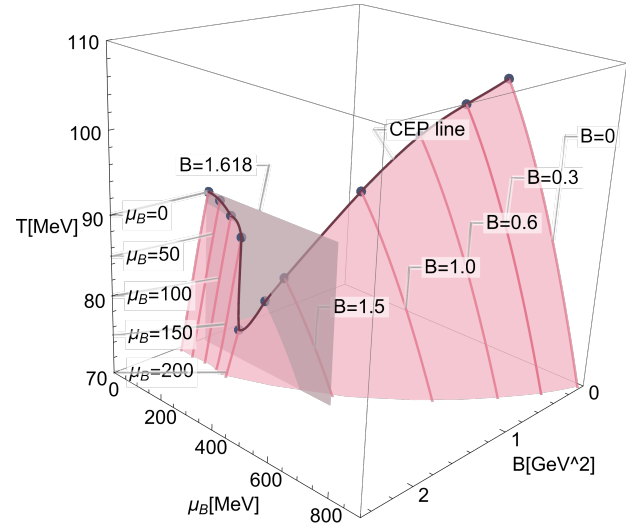


FIG. 3. The QCD phase diagram at finite magnetic field, temperature and baryon chemical potential using the holographic QCD model. The pink area is the first-order phase transition surface, and the red line is the CEP line.

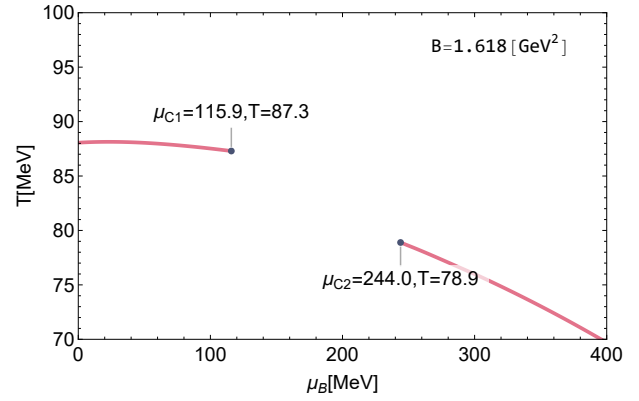


FIG. 4. QCD phase diagram in the $T - \mu_B$ plane for $B = 1.618 \text{ GeV}^2$. As μ_B increases, the first order line (red curve) terminates at $\mu_{C1} = 115.9 \text{ MeV}$ and transitions to a smooth crossover. The second CEP appears beyond a critical chemical potential $\mu_{C2} = 224.0 \text{ MeV}$.

There are four critical exponents that can be directly extracted from the phase diagram of Fig. 3.

- **Specific Heat Critical Exponent α** : The exponent α quantifies the power-law behavior of specific heat near a CEP along the axis defined as approaching the CEP approached along the tangent of the first-order line, i.e. the first-order axis. There are two ways extracting α :

$$C_n = T \left(\frac{\partial s}{\partial T} \right)_{n_B} \sim |T - T_{\text{CEP}}|^{-\alpha}.$$

$$C_M = T \left(\frac{\partial s}{\partial T} \right)_M \sim |T - T_{\text{CEP}}|^{-\alpha}.$$

- **Entropy Density Critical Exponent β :** It characterizes the discontinuity of entropy density s across the first-order line:

$$\Delta s = s_{>} - s_{<} \sim (T_{\text{CEP}} - T)^\beta,$$

where $s_{>}$ and $s_{<}$ represent the entropy densities in the high- and low-temperature phases, respectively.

- **Baryon Susceptibility Critical Exponent γ :** It represents the power-law behavior of baryon susceptibility with the temperature near the CEP along the first-order axis:

$$\chi_2^B = \frac{1}{T^2} \left(\frac{\partial n_B}{\partial \mu_B} \right)_T \sim |T - T_{\text{CEP}}|^{-\gamma}.$$

$$\chi_2^M = \frac{1}{T^2} \left(\frac{\partial M}{\partial B} \right)_T \sim |T - T_{\text{CEP}}|^{-\gamma}.$$

- **Critical Exponent δ along critical isotherm:** The definition of δ relies on the power-law relationship between entropy and chemical potential with $T = T_{\text{CEP}}$ at the critical isotherm:

$$s - s_{\text{CEP}} \sim |\mu_B - \mu_{B\text{CEP}}|^{1/\delta},$$

$$s - s_{\text{CEP}} \sim |B - B_{\text{CEP}}|^{1/\delta},$$

where s_{CEP} is the entropy density at the CEP.

Table I presents the set of critical exponents for CEP at three different magnetic fields, denoted by hQCD (I, II, III). The resulting critical exponents aligning with the scaling relations $\alpha + 2\beta + \gamma = 2$, $\alpha + \beta(1 + \delta) = 2$, providing a self-consistency check of our results. Although these critical exponents are closed to the one from mean-field theory, their values do depend on the location of CEP. The derivation becomes remarkable as B is increased. We highlight that the critical behavior cannot be attributed to large- N effects typically in conventional holographic duality. The later yields the critical behavior of mean field theory. Our holographic QCD model is constructed from 2+1-flavor lattice QCD data with $N_c = 3$. A notable example is the one in the holographic 2-flavor model [32], which coincides with the critical exponents of the quantum 3D Ising model, highlighting the unique characteristics of our holographic approach compared to conventional large- N QCD models.

Discussion—We start by outlining the pathway from observational data to deriving a holographic effective action, introducing a systematic approach that leverages neural networks to address the inverse problem. By employing this framework, we have developed a holographic model that incorporates magnetic effects to examine the phase diagram in (2+1)-flavor QCD.

	α	β	γ	δ
Experiment	0.110-0.116	0.316-0.327	1.23-1.25	4.6-4.9
3D Ising	0.110(5)	0.325±0.0015	1.2405±0.0015	4.82(4)
Mean field	0	1/2	1	3
DGR model	0	0.482	0.942	3.035
hQCD(I)	0.0046233	0.532779	0.91629	3.00825
hQCD(II)	0.0233477	0.481381	1.05119487	3.238166
hQCD(III)	0.019778	0.46259	1.03499	3.48613

TABLE I. Critical exponents from experiments in non-QCD fluids, the full quantum 3D Ising model, mean-field (van der Waals) theory, the DGR model [10], and our 2+1-flavor hQCD model. The hQCD (I, II, III) correspond to the critical exponents for $\mu_B = 554.66$ MeV, $B = 0$ (hQCD I), $\mu_B = 501.4$ MeV, $B = 0.3$ GeV² (hQCD II), and $\mu_B = 0$, $B = 1.6$ GeV² (hQCD III), respectively.

Our model accurately reproduces key thermodynamic behaviors, showing quantitative alignment with recent lattice QCD simulations at finite magnetic fields. It effectively captures critical elements of QCD transitions, such as a reliable first-order transition surface and the CEP line within the three-dimensional QCD phase diagram at finite μ_B and B . We find that the CEP temperature exhibits non-monotonic behavior, initially decreasing and then increasing with increasing magnetic field, which is reminiscent of the (inverse) magnetic catalysis. Surprisingly, for large B , in the T - μ_B plane, there exist two CEPs that converge to a single point as the magnetic field increases. Moreover, the first-order phase transition can happen at very small μ_B and thus could provide a potential source for a stochastic background of gravitational waves from the first-order QCD transition in the early universe, no worry about the sharp constrain on the baryon asymmetry through cosmological observations.

The phase diagram on the T - B plane is also provided. The CEP on the T - B plane at vanishing chemical potential aligns with current speculations in the lattice QCD literature. Close to the CEP, our model allows for the precise determination of various critical exponents, demonstrating adherence to scaling law relations. Interestingly, these critical exponents slightly deviate from conventional mean-field theory predictions, indicating unique behavior within the holographic context. Furthermore, our equation of state at finite density and magnetic field offers valuable insights to support experimental studies in QCD matter. In particular, we observe rich phase structure at relatively low values of μ_B with strong magnetic fields, for which the sign problem is probably surmountable and experiment facilities can cover easily. Therefore we expect that it will be possible to check our results either on the lattice simulations or from heavy-ion collisions.

Future research should focus on developing holographic models that incorporate asymptotic freedom and accurately capture QCD properties across energy scales. Additionally, we should improve the current model to

incorporate the associated thermodynamic and transport properties of the confining hadron resonance gas phase. Addressing these limitations can bridge the gap between theoretical predictions and experimental observations in heavy-ion collisions and astrophysical phenomena. Moreover, adopting a multidimensional approach that includes factors like isospin and rotation could offer deeper insights into underlying physics while investigating real-time dynamics in non-equilibrium scenarios may reveal novel phenomena and enhance our understanding of QCD matter dynamics.

Acknowledgements—We thank Heng-Tong Ding, Matti Järvinen, Elias Kiritsis, Zhibin Li, Yi-Bo Yang, Danning Li, Javier Subils, Ling-Xiao Wang, Shao-Jiang Wang, Yuan-Xu Wang, Yi Yang, and Peihung Yuan for stimulating discussions. This work is supported in part by the National Key Research and Development Program of China Grants No.2020YFC2201501 and No.2020YFC2201502, in part by the National Natural Science Foundation of China Grants No.12075101, No.12047569, No.12122513, No.12075298, No.11991052, No.12235016 and No.12047503. S.H. also would like to appreciate the financial support from the Max Planck Partner Group, the Fundamental Research Funds for the Central Universities.

Appendix A: Equations of motion

The form of $V(\phi)$ and $Z(\phi)$ is taken from [29].

$$\begin{aligned} V(\phi) &= -12 \cosh[c_1\phi] + (6c_1^2 - \frac{3}{2})\phi^2 + c_2\phi^6, \\ Z(\phi) &= \frac{1}{1+c_3} \operatorname{sech}[c_4\phi^3] + \frac{c_3}{1+c_3} e^{-c_5\phi}. \end{aligned} \quad (4)$$

By varying the action, the field equations can be obtained:

$$\begin{aligned} \nabla_\mu \nabla^\mu \phi - \frac{\partial_\phi Z}{4} F_{\mu\nu} F^{\mu\nu} - \frac{\partial_\phi \hat{Z}}{4} \hat{F}_{\mu\nu} \hat{F}^{\mu\nu} - \partial_\phi V &= 0 \\ \nabla^\nu (Z F_{\nu\mu}) &= 0 \\ \nabla^\nu (\hat{Z} \hat{F}_{\nu\mu}) &= 0 \\ R_{\mu\nu} - \frac{1}{2} R g_{\mu\nu} &= \frac{1}{2} \nabla_\mu \phi \nabla_\nu \phi + \frac{Z}{2} F_{\mu\rho} F_\nu^\rho + \frac{\hat{Z}}{2} \hat{F}_{\mu\rho} \hat{F}_\nu^\rho \\ + \frac{1}{2} \left(-\frac{1}{2} \nabla_\mu \phi \nabla^\mu \phi - \frac{Z}{4} F_{\mu\nu} F^{\mu\nu} - \frac{\hat{Z}}{4} \hat{F}_{\mu\nu} \hat{F}^{\mu\nu} - V \right) &g_{\mu\nu}. \end{aligned}$$

Expansion at the UV boundary $r \rightarrow \infty$ yields

$$\begin{aligned} \phi(r) &= \frac{\phi_s}{r} + \frac{(\phi_v + \frac{1}{6}(-1 + 6c_1^4)\phi_s^3 \ln[r])}{r^3} + \frac{B^2 \hat{Z}'(0)}{6r^4} + \dots, \\ g(r) &= 1 + \frac{g_4 - \frac{1}{4} B^2 \ln[r] \hat{Z}'(0)}{r^4} + \frac{B^2 \phi_s \hat{Z}'(0)}{5r^5} + \dots, \\ \eta(r) &= 1 + \frac{\phi_s^2}{6r^2} + \frac{g_4}{r^4} \\ &\quad + \frac{\frac{1}{144} \left((1 - 6c_1^4)\phi_s^4 + 72\phi_s \phi_v + 12B^2 \hat{Z}'(0) \right)}{r^4} \\ &\quad + \frac{\frac{1}{12} \ln[r] \left(-((1 - 6c_1^4)\phi_s^4) - 3B^2 \hat{Z}'(0) \right)}{r^4} \\ &\quad + \frac{16B^2 \phi_s \hat{Z}'(0)}{45r^5} + \dots, \\ A(r) &= \mu_B - \frac{2\kappa_N^2 n_B}{2r^2} + \frac{2\kappa_N^2 n_B \phi_s Z'(0)}{3r^3 Z(0)} \\ &\quad + \frac{2\kappa_N^2 n_B \phi_s^2 (Z(0)^2 - 12Z'(0)^2 + 6Z(0)Z''(0))}{48r^4 Z(0)^2} + \dots, \end{aligned} \quad (5)$$

where we have taken the normalization of the spacetime coordinates at the boundary such that $\eta(r \rightarrow \infty) = 0$ and $g(r \rightarrow \infty) = 1$.

Expansion at the event horizon $r = r_h$ gives

$$\begin{aligned} f &= f_h(r - r_h) + \dots, \\ \eta &= \eta_h + \eta_1(r - r_h) + \dots, \\ A &= A_h(r - r_h) + \dots, \\ \phi &= \phi_h + \phi_1(r - r_h) + \dots, \\ g &= g_h + g_1(r - r_h) + \dots. \end{aligned} \quad (6)$$

After substituting (6) into the equations of motion, one finds five independent coefficients $(r_h, A_h, \eta_h, \phi_h, g_h)$.

The relationship between the free energy Ω and the on-shell action S is:

$$-\Omega V = T(S + S_\partial)_{on-shell}, \quad (7)$$

where V is the spatial volume of the boundary system. The boundary term is given by

$$\begin{aligned} S_\partial &= \frac{1}{2\kappa_N^2} \int_{r \rightarrow \infty} d^4x \sqrt{-h} \left[2K - 6 - \frac{1}{2} \phi(r)^2 \right. \\ &\quad \left. - \left(\frac{6c_1^4 - 1}{12} \right) \phi(r)^4 \ln[r] - b\phi(r)^4 \right. \\ &\quad \left. + \frac{1}{4} (F_{\mu\nu} F^{\mu\nu} + \hat{Z}(0) \hat{F}_{\mu\nu} \hat{F}^{\mu\nu}) \ln[r] \right]. \end{aligned} \quad (8)$$

Here $h_{\mu\nu}$ is the induced metric at the UV boundary with $K_{\mu\nu}$ the extrinsic curvature defined by the outward pointing normal vector to the boundary.

The boundary energy-momentum tensor reads

$$\begin{aligned}
T_{\mu\nu} &= \lim_{r \rightarrow \infty} \frac{2r^2}{\sqrt{-h}} \frac{\delta(S + S_\partial)}{\delta h^{\mu\nu}} \\
&= \frac{1}{2\kappa_N^2} \lim_{r \rightarrow \infty} r^2 \left[2(Kh_{\mu\nu} - K_{\mu\nu} - 3h_{\mu\nu}) - \left(\frac{1}{2}\phi^2 \right. \right. \\
&\quad \left. \left. + \frac{6c_1^4 - 1}{12}\phi^4 \ln[r] + b\phi^4\right)h_{\mu\nu} \right. \\
&\quad \left. - (F_{\mu\rho}F_{\nu}^\rho - \frac{1}{4}h_{\mu\nu}F_{\rho\lambda}F^{\rho\lambda}) \ln[r] \right. \\
&\quad \left. - \hat{Z}(0)(\hat{F}_{\mu\rho}\hat{F}_{\nu}^\rho - \frac{1}{4}h_{\mu\nu}\hat{F}_{\rho\lambda}\hat{F}^{\rho\lambda}) \ln[r] \right]
\end{aligned} \tag{9}$$

Substituting the expansion on the boundary gives:

$$\begin{aligned}
\epsilon = T_{tt} \\
&= \frac{(1 + 48b)\phi_s^4}{96\kappa_N^2} + \frac{\phi_s\phi_v}{2\kappa_N^2} + \frac{-144f_v + 192g_4 + 12B^2\hat{Z}[0]}{96\kappa_N^2}
\end{aligned} \tag{10}$$

$$\begin{aligned}
p_x = p_y = T_{xx} = T_{yy} \\
&= \frac{(3 - 48b - 8c_1^4)\phi_s^4}{96\kappa_N^2} + \frac{\phi_s\phi_v}{2\kappa_N^2} + \frac{-48f_v - 8B^2\hat{Z}[0]}{96\kappa_N^2}
\end{aligned} \tag{11}$$

$$\begin{aligned}
-\Omega = p_z = T_{zz} &= \frac{(3 - 48b - 8c_1^4)\phi_s^4}{96\kappa_N^2} \\
&\quad + \frac{\phi_s\phi_v}{2\kappa_N^2} + \frac{-48f_v + 4(48g_4 + B^2\hat{Z}[0])}{96\kappa_N^2}.
\end{aligned} \tag{12}$$

Note that in the thermodynamic limit $V \rightarrow \infty$, $\Omega = -p_z$. From the equations of motion, we can get a radially conserved charge:

$$\begin{aligned}
Q &= e^{\frac{\eta(r)}{2}} \sqrt{g(r)} r^3 \left(r^2 \left(e^{-\frac{\eta(r)}{2}} \frac{f(r)}{r^2} \right)' - Z(\phi)A(r)A'(r) \right) \\
&\quad - B^2 \int_{r_h}^r \frac{e^{-\frac{\eta(r_s)}{2}} \sqrt{g(r_s)} \hat{Z}[\phi(r_s)]}{r_s} dr_s,
\end{aligned} \tag{13}$$

which connects data from the horizon to the UV boundary. Evaluating it at both horizon and the boundary yields and it is at the horizon:

$$Q = Ts = \epsilon - \Omega - \mu_B n_B = \epsilon^{total} - \Omega - \mu_B n_B - BM, \tag{14}$$

where $\epsilon^{total} = \epsilon + \epsilon^{field}$ is the total energy including the external field $\epsilon^{field} = BM$ with M the magnetization. This is the the expected thermodynamic relation. More precisely, M can be computed by the partial derivative of the free energy with respect to B .

$$\begin{aligned}
M &= -\frac{\partial\Omega}{\partial B} = -\int_{r_h}^{\infty} \frac{B\sqrt{e^{-\eta(r)}g(r)}\hat{Z}[\phi(r)]}{r} dr \\
&\quad + \lim_{r \rightarrow \infty} \frac{B\sqrt{e^{-\eta(r)}f(r)g(r)}\ln[r]\hat{Z}[0]}{r}
\end{aligned} \tag{15}$$

. It can be checked straightforwardly that the the first law of thermodynamics

$$d\Omega = -sdT - n_B d\mu_B - MdB \tag{16}$$

is satisfied.

Following [29], we choose $c_1 = 0.7100, c_2 = 0.0037, c_3 = 1.935, c_4 = 0.085, c_5 = 30$ of (4). Moreover, we take $\kappa_N^2 = 2\pi(1.68), \phi_s = 1085\text{MeV}$ and $b = -0.27341$.

Appendix B: Calculation method and neural ODEs

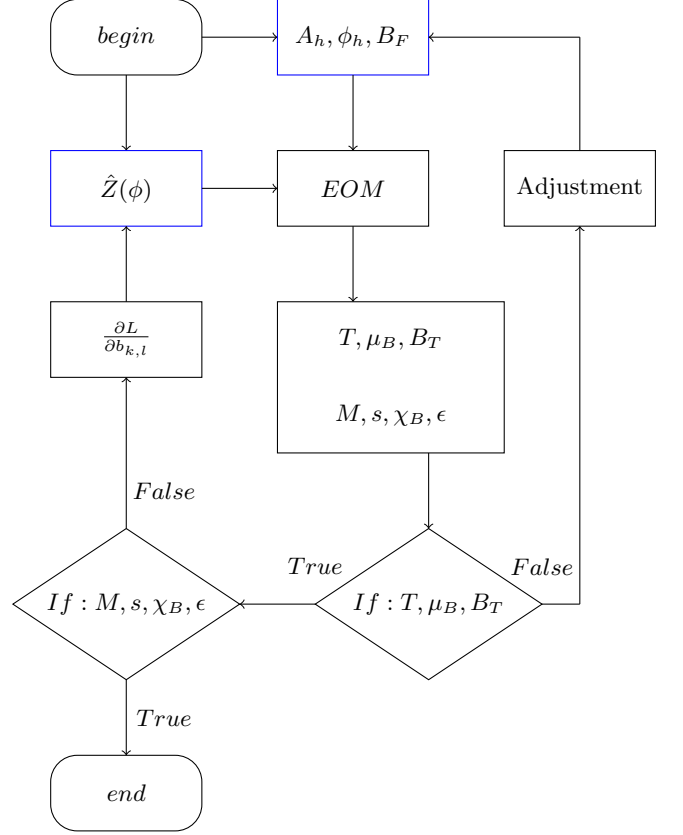


FIG. 5. Algorithm process: Given a trial functional $\hat{Z}(\phi)$ and a set of A_h, ϕ_h, B_F , solve the equations of motion to obtain the thermodynamic quantities $T, \mu_B, B_T, M, S, \chi_B, \epsilon$. Verify whether these T, μ_B, B_T cover the range of lattice QCD data. If not, adjust A_h, ϕ_h, B_F . If they do, compare this set with the corresponding lattice data for M, S, χ_B, ϵ . If consistent, terminate the process. If not, adjust $\hat{Z}(\phi)$ and repeat the process. Adjustments to $\hat{Z}(\phi)$ are made through gradient descent, where L represents the loss function and $b_{k,l}$ are the network parameters used to mimic $\hat{Z}(\phi)$. $\frac{\partial L}{\partial b_{k,l}}$ indicates the direction of descent for the loss function. When the loss function reaches its minimum, it signifies the optimal solution for the $\hat{Z}(\phi)$ function.

The neural network and neural ODEs have been applied in the holographic literature e.g. [33–36]. In our

current situation, We extend the neural ODEs to numerically solve the magnetic coupling $\hat{Z}[\phi(z)]$, which can be constrained by lattice QCD data in a high precision. In this section, we present the necessary details to make the results fully reproducible.

Our computational approach is illustrated in Fig. 5. To address the inverse problem of translating lattice QCD data into a holographic model, we initialize a randomly selected trial function $\hat{Z}(\phi)$. This function is used to obtain a gravitational solution to the equations of motion, adhering to asymptotic AdS boundary conditions and regular boundary conditions at the horizon. Once the solution is obtained, we extract the boundary field theory observables, compare them with lattice QCD data, and subsequently refine the trial function $\hat{Z}(\phi)$.

Thanks to the scaling symmetries, there are three independent IR data points, namely A_h , ϕ_h , and B_F , which represent the values of the fields A and ϕ at the event horizon, and the pre-scale-transformed magnetic field B_F . These three degrees of freedom correspond to the UV data: temperature (T), chemical potential (μ_B), and the magnetic field (B_T) of the boundary field theory, where B_T denotes the physical magnetic field after scale transformation due to scaling symmetry. By applying a neural network to mimic the trial function $\hat{Z}(\phi)$, we solve the equations of motion and subsequently obtain the thermodynamic quantities of the boundary field theory, including T , μ_B , B_T , M , s , χ_B , and ϵ .

Since the lattice data [22] covers only a small region at zero chemical potential, the values of T , μ_B , and B_T computed with an arbitrary set of A_h , ϕ_h , and B_F cannot adequately cover this region. Therefore, as shown in Fig. 5, it is necessary to adjust A_h , ϕ_h , and B_F to obtain a set that effectively covers the relevant lattice QCD region. The values of the remaining thermodynamic quantities M , S , χ_B , and ϵ depend on the choice of the trial function $\hat{Z}(\phi)$.

To optimize $\hat{Z}(\phi)$, we define a loss function $L = L(M, s, \chi_B, \epsilon)$. We can obtain the optimal $\hat{Z}(\phi)$ by iteratively applying gradient descent to minimize the loss function. Since our model's high precision requirements, we have to employ a neural network ODE model [37] to solve for $\hat{Z}(\phi)$ throughout the entire process. This model effectively transforms the conventional neural network into a continuous form, facilitating differential equations' rapid and accurate solutions.

For later convenience, one can rephrase the equations of motion eq.(2) as the following form:

$$\frac{d\Theta}{dz} = \Xi(z, \Theta, \dot{\Theta}(z), \hat{Z}(\Phi), B_F), \Theta(z) = \begin{pmatrix} \Phi(z) \\ F(z) \\ \eta(z) \\ A(z) \\ g(z) \end{pmatrix} \quad (17)$$

Where the $\dot{\Theta}(z)$ is to take the derivative with respect to the argument and $z = 1/r$, $z\Phi(z) = \phi(\frac{1}{z})$, $F(z) =$

$z^2 f(\frac{1}{z})$, $A(z) = A_t(\frac{1}{z})$. One can refer to the precise definitions of these functions in eq.(2). Ξ is a five-component vector. Θ contains scalar field ϕ , metric components f , g , η , and Maxwell field A_t . These equations of motion (17) can be rewritten as a discrete difference equation which can be realized by the neural network as shown in Fig. 6:

$$\Theta_{i+1} = \Theta_i + \Xi(z_i, \Theta_i, \dot{\Theta}(z), \hat{Z}(\Phi_i), B_F)dz, \quad (18)$$

where we discretize the holographic direction z with a step size dz . The index i corresponds to the i -th layer. The equation gives the recursive relationship between the i -th layer and the $i+1$ -th layer. Θ_i is correspond to the field value at the i -th layer. Here, $i = 1$ represents the event horizon, and $i = N$ corresponds to the UV boundary. In our setup, we choose $6 \times N$ neural network to replace the difference equations.

Here, we selected four thermodynamically independent data sets \mathcal{S} that contain quantities $\mathcal{S} = \{M, s, \chi_B, \epsilon\}$ for an accurate comparison between the holographic model and Lattice QCD data, performing a global fitting. Through this global fitting, we obtained the numerical solution $\hat{Z}(\phi)$ that minimizes the loss function. The comparison results between the holographic model and Lattice QCD data are presented in the main text, with all detailed comparison plots provided in the appendix. We choose loss function $L = L(M, s, \chi_B, \epsilon)$ as mean-square error (MSE).

The problem is to minimize the loss function by optimizing the functional $\hat{Z}(\phi)$. To determine the optimizing direction of $\hat{Z}(\phi)$, one needs backpropagation of the neural network to extract the data associated with $\frac{\partial L}{\partial b_{i,j}}$. The precise form of loss function L is

$$L = \sum_{I \in \mathcal{S}} p_I (I_{\text{LQCD}} - I_{\text{HQCD}})^2 \quad (19)$$

where $I_{\text{LQCD}}, I_{\text{HQCD}}$ correspond to the thermal dynamical quantities \mathcal{S} of lattice QCD data and are predicted by holographic QCD respectively. p_I is the artificial weight number to keep the amplitude of $p_I (I_{\text{LQCD}} - I_{\text{HQCD}})^2$ to be the same order.

To minimize the loss function, we have to input $\frac{\partial L}{\partial b_{k,l}}$ and $b_{k,l}$ into Adam($\alpha = 0.0002, \beta_1 = 0.9, \beta_2 = 0.999$) [38]. The key issue is to collect the data $\frac{\partial L}{\partial b_{k,l}}$ for Adam. For the i -th layer, we have the following chain rule:

$$\frac{\partial L}{\partial b_{k,l}} = \frac{\partial L}{\partial \Theta_{i+1}} \frac{\partial \Theta_{i+1}}{\partial b_{k,l}}, \quad (20)$$

Here one has to note that the neural $b_{k,l}$ in each layer are the same. Due to eq.(18) at the each layer, it can be expressed by

$$\frac{\partial L}{\partial b_{k,l}} = \frac{\partial L}{\partial \Theta_{i+1}} \frac{\partial \Xi(z_i, \Theta_i, Z(\Phi_i), B_F)}{\partial b_{k,l}} dz \quad (21)$$

Finally, for the whole network, the key ingredient $\frac{\partial L}{\partial b_{k,l}}$ is:

$$\frac{\partial L}{\partial b_{k,l}} = \int \frac{\partial L}{\partial \Theta} \frac{\partial \Xi}{\partial b_{k,l}} dz \quad (22)$$

To obtain the first factor of the integrant in the eq.(22), we can make use of the following chain rule for the two neighborhood layers:

$$\frac{\partial L}{\partial \Theta_i} = \frac{\partial L}{\partial \Theta_{i+1}} \frac{\partial \Theta_{i+1}}{\partial \Theta_i} \quad (23)$$

where $\frac{\partial L}{\partial \Theta_i}$ represents the derivative of each component in Θ at the i -th layer, with the component index omitted for clarity. Here, $\frac{\partial \Theta_{i+1}}{\partial \Theta_i}$ is a 5×5 matrix. From Eq. (18), we obtain:

$$\begin{aligned} \frac{\partial L}{\partial \Theta_i} &= \frac{\partial L}{\partial \Theta_{i+1}} \frac{\partial \Theta_{i+1}}{\partial \Theta_i} \\ &= \frac{\partial L}{\partial \Theta_{i+1}} \left(1 + \frac{\partial \Xi(z_i, \Theta_i, \dot{\Theta}_i(z), \hat{Z}(\Phi_i), B_F)}{\partial \Theta_i} dz \right) \end{aligned} \quad (24)$$

For convenience, let y_i denote $\frac{\partial L}{\partial \Theta_i}$. Then, Eq. (24) can be written as:

$$y_i = y_{i+1} \left(1 + \frac{\partial \Xi(z_i, \Theta_i, \dot{\Theta}_i(z), \hat{Z}(\Phi_i), B_F)}{\partial \Theta_i} dz \right) \quad (25)$$

The above difference equation corresponds to the following differential form:

$$y'(z) = -y(z) \frac{\partial \Xi(z, \Theta, \dot{\Theta}_i(z), \hat{Z}(\Phi), B_F)}{\partial \Theta} \quad (26)$$

To simplify our notations, we note that this set of equations involves five unknown functions as shown in the eq.(17), and $\frac{\partial \Xi}{\partial \Theta}$ is a 5×5 matrix.

Finally, we combine all the elements in Eq. (22) and input them into the Adam optimizer to achieve the functional $\hat{Z}(\phi)$, which is a crucial point of this work. Once we obtain the numerical data for $\hat{Z}(\phi)$, its approximate analytical form is:

$$\begin{aligned} \hat{Z}(\phi) &= b_0 \exp[-b_1(\phi - b_2)^2] \\ &\quad + b_3 \exp[-b_4(\phi - b_5)^2 - b_6(\phi - b_7)^4] \\ &\quad + b_8 \operatorname{sech}[-b_9(\phi - b_{10})^2] \\ &\quad + b_{11} \exp[-b_{12}(\phi - b_{13})^6] + b_{14}, \end{aligned} \quad (27)$$

where the parameters are given by:

$$\begin{aligned} b_0 &= \frac{49677}{100000}, & b_1 &= \frac{8583}{25000}, & b_2 &= \frac{202953}{100000}, \\ b_3 &= \frac{15371}{50000}, & b_4 &= \frac{6297}{50000}, & b_5 &= \frac{39131}{20000}, \\ b_6 &= \frac{411}{50000}, & b_7 &= \frac{413981}{100000}, & b_8 &= \frac{97}{4000}, \\ b_9 &= \frac{34873}{100000}, & b_{10} &= \frac{29503}{50000}, & b_{11} &= -\frac{287}{50000}, \\ b_{12} &= \frac{24319}{12500}, & b_{13} &= \frac{2637}{2500}, & b_{14} &= -\frac{691}{50000}. \end{aligned} \quad (28)$$

To illustrate the efficacy of the algorithm, we present a comparison of four thermodynamically independent quantities, $\mathcal{S} = \{M, s, \chi_B, \epsilon\}$, between the holographic predictions and the lattice QCD simulations, as shown in Fig. 1. Additionally, we confirm that the corresponding trace anomaly I , the renormalized longitudinal pressure ΔP_z , and the renormalized anomaly ΔI predicted by the holographic model align with the lattice QCD data [22], as presented in Fig. 8. This work represents the first quantitative realization of state-of-the-art lattice QCD data [22] within a holographic model.

* cairg@itp.ac.cn,
hesong@jlu.edu.cn,
liliphy@itp.ac.cn,
zengha20@mails.jlu.edu.cn

- [1] P. Braun-Munzinger and J. Wambach, ‘‘The Phase Diagram of Strongly-Interacting Matter,’’ *Rev. Mod. Phys.* **81** (2009), 1031-1050 [arXiv:0801.4256 [hep-ph]].
- [2] O. Philipsen, ‘‘The QCD equation of state from the lattice,’’ *Prog. Part. Nucl. Phys.* **70** (2013), 55-107 [arXiv:1207.5999 [hep-lat]].
- [3] S. Gupta, X. Luo, B. Mohanty, H. G. Ritter and N. Xu, ‘‘Scale for the Phase Diagram of Quantum Chromodynamics,’’ *Science* **332** (2011), 1525-1528 [arXiv:1105.3934 [hep-ph]].
- [4] J. O. Andersen, W. R. Naylor and A. Tranberg, ‘‘Phase diagram of QCD in a magnetic field: A review,’’ *Rev. Mod. Phys.* **88**, 025001 (2016) [arXiv:1411.7176 [hep-ph]].
- [5] V. A. Miransky and I. A. Shovkovy, *Phys. Rept.* **576** (2015), 1-209 [arXiv:1503.00732 [hep-ph]].
- [6] T. Demircik, C. Ecker and M. Järvinen, *Phys. Rev. X* **12** (2022) no.4, 041012 [arXiv:2112.12157 [hep-ph]].
- [7] Y. Chen, D. Li and M. Huang, *Commun. Theor. Phys.* **74** (2022) no.9, 097201 [arXiv:2206.00917 [hep-ph]].
- [8] R. Rougemont, J. Grefa, M. Hippert, J. Noronha, J. Noronha-Hostler, I. Portillo and C. Ratti, *Prog. Part. Nucl. Phys.* **135** (2024), 104093 doi:10.1016/j.pnpnp.2023.104093 [arXiv:2307.03885 [nucl-th]].
- [9] S. S. Gubser, A. Nellore, S. S. Pufu and F. D. Rocha, ‘‘Thermodynamics and bulk viscosity of approximate black hole duals to finite temperature quantum chromodynamics,’’ *Phys. Rev. Lett.* **101** (2008), 131601 [arXiv:0804.1950 [hep-th]].
- [10] O. DeWolfe, S. S. Gubser and C. Rosen, ‘‘A holographic critical point,’’ *Phys. Rev. D* **83** (2011), 086005 [arXiv:1012.1864 [hep-th]].
- [11] O. DeWolfe, S. S. Gubser and C. Rosen, ‘‘Dynamic critical phenomena at a holographic critical point,’’ *Phys. Rev. D* **84** (2011), 126014 [arXiv:1108.2029 [hep-th]].
- [12] U. Gursoy, M. Jarvinen and G. Nijs, ‘‘Holographic QCD in the Veneziano Limit at a Finite Magnetic Field and Chemical Potential,’’ *Phys. Rev. Lett.* **120** (2018) no.24, 242002 [arXiv:1707.00872 [hep-th]].
- [13] J. Grefa, J. Noronha, J. Noronha-Hostler, I. Portillo, C. Ratti and R. Rougemont, ‘‘Hot and dense quark-gluon plasma thermodynamics from holographic black holes,’’

- Phys. Rev. D **104** (2021) no.3, 034002 [arXiv:2102.12042 [nucl-th]].
- [14] S. He, S. Y. Wu, Y. Yang and P. H. Yuan, “Phase Structure in a Dynamical Soft-Wall Holographic QCD Model,” JHEP **04** (2013), 093 [arXiv:1301.0385 [hep-th]].
- [15] T. Alho, M. Järvinen, K. Kajantie, E. Kiritsis, C. Rosen and K. Tuominen, “A holographic model for QCD in the Veneziano limit at finite temperature and density,” JHEP **04** (2014), 124 [erratum: JHEP **02** (2015), 033] [arXiv:1312.5199 [hep-ph]].
- [16] J. Knaute, R. Yaresko and B. Kämpfer, “Holographic QCD phase diagram with critical point from Einstein–Maxwell-dilaton dynamics,” Phys. Lett. B **778** (2018), 419–425 [arXiv:1702.06731 [hep-ph]].
- [17] R. Critelli, J. Noronha, J. Noronha-Hostler, I. Portillo, C. Ratti and R. Rougemont, “Critical point in the phase diagram of primordial quark-gluon matter from black hole physics,” Phys. Rev. D **96** (2017) no.9, 096026 [arXiv:1706.00455 [nucl-th]].
- [18] Y. Yang and P. H. Yuan, “QCD Phase Diagram by Holography,” [arXiv:2011.11941 [hep-th]].
- [19] R. G. Cai, S. He and D. Li, “A hQCD model and its phase diagram in Einstein-Maxwell-Dilaton system,” JHEP **03** (2012), 033 [arXiv:1201.0820 [hep-th]].
- [20] S. I. Finazzo, R. Critelli, R. Rougemont and J. Noronha, Phys. Rev. D **94** (2016) no.5, 054020 [arXiv:1605.06061 [hep-ph]].
- [21] A. Bazavov *et al.* [HotQCD], “Equation of state in (2+1)-flavor QCD,” Phys. Rev. D **90** (2014), 094503 [arXiv:1407.6387 [hep-lat]].
- [22] G. S. Bali, F. Bruckmann, G. Endrödi, S. D. Katz and A. Schäfer, JHEP **08**, 177 (2014) [arXiv:1406.0269 [hep-lat]].
- [23] In most studies, e.g. [13, 16–18], the thermodynamic variables were obtained by integrating the standard first law of thermodynamics, whose validity is still under investigation for AdS black holes with scalar hair [24–27].
- [24] L. Li, “On Thermodynamics of AdS Black Holes with Scalar Hair,” Phys. Lett. B **815** (2021), 136123 [arXiv:2008.05597 [gr-qc]].
- [25] T. Hertog and G. T. Horowitz, “Designer gravity and field theory effective potentials,” Phys. Rev. Lett. **94**, 221301 (2005) [arXiv:hep-th/0412169 [hep-th]].
- [26] A. Anabalón, D. Astefanesei, D. Choque and C. Martinez, “Trace Anomaly and Counterterms in Designer Gravity,” JHEP **03**, 117 (2016) [arXiv:1511.08759 [hep-th]].
- [27] H. Lu, C. N. Pope and Q. Wen, “Thermodynamics of AdS Black Holes in Einstein-Scalar Gravity,” JHEP **03**, 165 (2015) [arXiv:1408.1514 [hep-th]].
- [28] S. Borsányi, Z. Fodor, J. N. Guenther, R. Kara, S. D. Katz, P. Parotto, A. Pásztor, C. Ratti and K. K. Szabó, “Lattice QCD equation of state at finite chemical potential from an alternative expansion scheme,” Phys. Rev. Lett. **126** (2021) no.23, 232001 [arXiv:2102.06660 [hep-lat]].
- [29] R. G. Cai, S. He, L. Li and Y. X. Wang, Phys. Rev. D **106** (2022) no.12, L121902 [arXiv:2201.02004 [hep-th]].
- [30] Z. Li, J. Liang, S. He and L. Li, “Holographic study of higher-order baryon number susceptibilities at finite temperature and density,” Phys. Rev. D **108**, no.4, 046008 (2023) [arXiv:2305.13874 [hep-ph]].
- [31] F. Cuteri, “QCD thermodynamics: an overview of recent progress,” PoS **LATTICE2022** (2023), 243 doi:10.22323/1.430.0243
- [32] Y. Q. Zhao, S. He, D. Hou, L. Li and Z. Li, Phys. Rev. D **109** (2024) no.8, 086015 [arXiv:2310.13432 [hep-ph]].
- [33] K. Li, Y. Ling, P. Liu and M. H. Wu, Phys. Rev. D **107**, no.6, 066021 (2023) [arXiv:2209.05203 [hep-th]].
- [34] K. Hashimoto, S. Sugishita, A. Tanaka and A. Tomiya, Phys. Rev. D **98**, no.10, 106014 (2018) [arXiv:1809.10536 [hep-th]].
- [35] B. Ahn, H. S. Jeong, K. Y. Kim and K. Yun, JHEP **03**, 141 (2024) [arXiv:2401.00939 [hep-th]].
- [36] X. Chen and M. Huang, Phys. Rev. D **109** (2024) no.5, L051902 [arXiv:2401.06417 [hep-ph]].
- [37] R. T. Q. Chen, Y. Rubanova, J. Bettencourt, and D. K. Duvenaud, “Neural Ordinary Differential Equations,” Advances in Neural Information Processing Systems, vol. 31, 2018.
- [38] Kingma, D. P., Ba, J., “Adam: A method for stochastic optimization,” [arXiv:1412.6980].

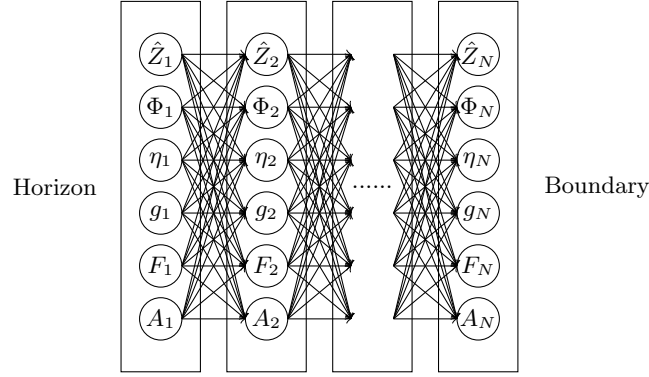


FIG. 6. Neural network representation of the recursive relationship between layers in solving the equations of motion eq.(17). The initial conditions are set at the event horizon ($i = 1$), and the layers extend to the UV boundary ($i = N$). Each layer i corresponds to the field values at that layer, with Θ_i representing the collective set of fields. The neural network approximates the continuous holographic direction z with discrete steps dz , optimizing the trial function $\hat{Z}(\phi)$ through gradient descent to minimize the loss function L .

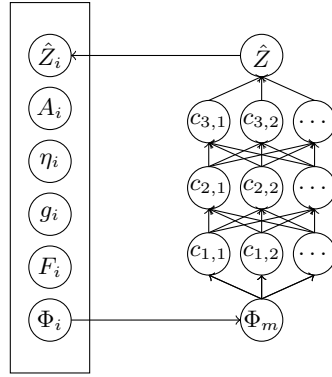


FIG. 7. The neural network representation of $\hat{Z}(\Phi)$: The function to be solved $\hat{Z}(\Phi)$ can be represented by a neural network, where Φ is the scalar field on the holographic direction, $c_{1,1}, c_{1,2}, \dots$ are the parameters of the neural network, for simplicity, only two layers of the network are drawn with six parameters, and the actual parameters reach hundreds. The neural network is a three-layer fully connected layer. Changing the parameters $c_{1,1}, c_{1,2}, \dots$ can change the function form of $\hat{Z}(\Phi)$. Since a two-layer neural network with enough parameters can fit any function, we do not need to discuss the specific form of $\hat{Z}(\Phi)$. Take any initial values of $c_{1,1}, c_{1,2}, \dots$ and iterate to solve.

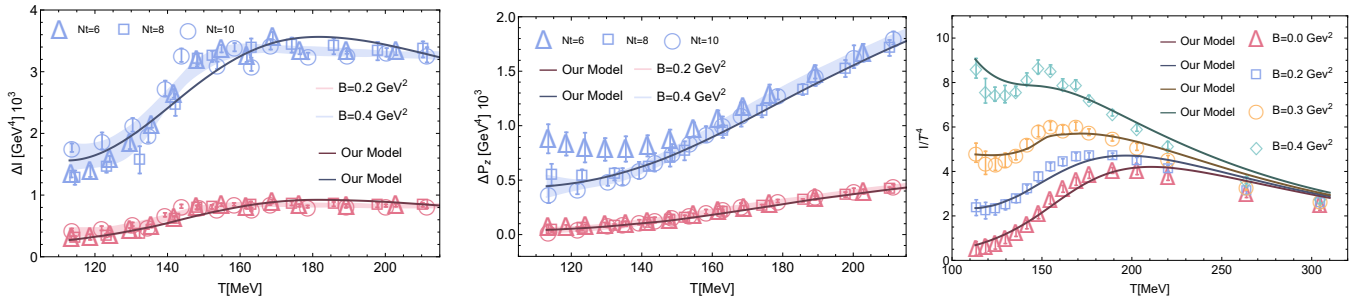


FIG. 8. The renormalized trace anomaly ΔI (left), the renormalized longitudinal pressure ΔP_z (middle) and the trace anomaly I (right). Our holographic computations (solid curves) are compared with the latest lattice QCD results from [22]. The Nt corresponds to three lattice spacings and B denotes the magnetic field strength. The shaded areas correspond to lattice continuum estimates.